

Contents lists available at ScienceDirect

# Petroleum Science

journal homepage: www.keaipublishing.com/en/journals/petroleum-science



# Original Paper

# Pore-scale gas—water two-phase flow and relative permeability characteristics of disassociated hydrate reservoir



Yu-Xuan Xia <sup>a</sup>, Derek Elsworth <sup>b</sup>, Sai Xu <sup>c</sup>, Xuan-Zhe Xia <sup>a</sup>, Jian-Chao Cai <sup>a, \*</sup>, Cheng Lu <sup>d, \*\*</sup>

- <sup>a</sup> State Key Laboratory of Petroleum Resources and Engineering, China University of Petroleum (Beijing), Beijing, 102249, China
- b Department of Energy and Mineral Engineering, G3 Center and Energy Institute, The Pennsylvania State University, University Park, 16802, PA, United States
- <sup>c</sup> Oil & Gas Technology Research Institute, Changqing Oilfield Company, CNPC, Xi'an, 710018, Shaanxi, China
- <sup>d</sup> Center of Oil & Natural Gas Resource Exploration, China Geological Survey, Beijing, 100083, China

#### ARTICLE INFO

#### Article history: Received 17 February 2025 Received in revised form 29 April 2025 Accepted 29 April 2025 Available online 30 April 2025

Edited by Yan-Hua Sun

Keywords: Clayey-silt reservoir Gas—water two-phase flow CT scanning Relative permeability Pore network model

#### ABSTRACT

Clayey-silt natural gas hydrate reservoirs in the South China Sea exhibit loose and unconsolidated structures, heterogeneous pore structures, high clay mineral contents, and strong hydrophilicity. These characteristics complicate the gas-water two-phase flow process in porous media following hydrate decomposition, posing challenges for efficient development. This study examines the transport response of clayey-silt reservoir samples from the Shenhu area using gas-water two-phase flow experiments and CT scanning to explore changes in pore structure, gas-water distribution, and relative permeability under varying flow conditions. The results indicate that pore heterogeneity significantly influences flow characteristics. Gas preferentially displaces water in larger pores, forming fracture-like pores, which serve as preferential flow channels for gas migration. The preferential flow channels enhance gas-phase permeability up to 19 times that of the water phase when fluid pressures exceed total stresses. However, small pores retain liquid, leading to a high residual water saturation of 0.561. CT imaging reveals that these hydro-fractures improve gas permeability but also confine gas flow to specific channels. Pore network analysis shows that gas injection expands the pore-throat network, enhancing connectivity and forming fracture-like pores. Residual water remains trapped in smaller pores and throats, while structural changes, including new fractures, improve gas flow pathways and overall connectivity. Relative permeability curves demonstrate a narrow gas-water cocurrent-flow zone, a right-shifted iso-permeability point and high reservoir capillary pressure, indicating a strong "water-blocking" effect. The findings suggest that optimizing reservoir stimulation techniques to enhance fracture formation, reduce residual water saturation, and improve gas flow capacity is critical for efficient hydrate reservoir development.

© 2025 The Authors. Publishing services by Elsevier B.V. on behalf of KeAi Communications Co. Ltd. This is an open access article under the CC BY license (http://creativecommons.org/licenses/by/4.0/).

#### 1. Introduction

Natural gas hydrates, as an abundant and highly efficient clean energy source (Sloan, 2003; Makogon et al., 2007; Waite et al., 2009), hold immense potential economic benefits. Since 2003, the China Geological Survey has explored and evaluated the resource of natural gas hydrates in the Shenhu area of the South China Sea, conducting geological, geophysical, and drilling investigations. In 2017 and 2020, the first exploratory production test

E-mail addresses: caijc@cup.edu.cn (J.-C. Cai), jaluch@126.com (C. Lu).

and the second experimental production test of natural gas hydrates in the South China Sea were conducted using the depressurization method (Li et al., 2018; Ye et al., 2020), laying a foundation for the potential industrial development of natural gas hydrate resources. During the production tests, issues such as high initial gas production rates followed by rapid declines, difficulties in maintaining stable output, and low water production were observed. These observations identify that multiphase flow characteristics in the reservoir during hydrate development remain unclear. The natural gas hydrate reservoirs in the South China Sea are primarily composed of clayey-silts and are characterized by unconsolidated deposits with high clay contents, strong waterwettability (Zhang et al., 2017; Dong et al., 2020; Qin et al., 2020)

<sup>\*</sup> Corresponding author.

<sup>\*\*</sup> Corresponding author.

and as such are structurally unstable during recovery (Wang et al., 2024). These characteristics make understanding of the dissociation then flow of the gas—water two-phase increasingly complex—especially at the dissociation front. And requiring that such issues are resolved to allow successful production (Zhang et al., 2021; Lu et al., 2023; Chen et al., 2024). Thus, clarifying the gas—water two-phase flow characteristics is a critical scientific issue that urgently needs to be addressed for the scientific and efficient development of hydrate resources.

The difficulty in obtaining undisturbed samples, the complexity and difficulty in completing two-phase dissociation-flow experiments result in only limited observations. Despite these constraints, certain progress has been made in understanding gas-water two-phase flow in hydrate-bearing sediments through experimental and numerical approaches. Experimental studies have provided insights into relative permeability and flow behavior under varying conditions. For instance, observations from in situ hydrate-bearing sediments demonstrate the influence of gas saturation distribution on relative permeability curves (Winters et al., 2011), while experiments with artificially synthesized methane hydrates reveal piston-like displacement patterns during twophase flow processes (Johnson et al., 2011). Additionally, variations in hydrate saturation have been shown to significantly affect relative permeability curves, emphasizing the intricate interplay between hydrate content and flow characteristics (Ahn et al., 2005). These studies collectively highlight the complexity of gas-water two-phase flow characteristics in porous sediments, with different research efforts yielding varying conclusions due to differences in experimental conditions, sediment properties, and fluid distribution. This variability underscores the challenges in generalizing two-phase flow behavior across diverse sedimentary

Numerical simulations have complemented these experimental efforts, offering a more detailed understanding of multiphase flow processes at various scales. Pore network models (PNM) have proven effective in simulating parameters such as gas entry pressure and water retention (Mahabadi et al., 2016; Ai et al., 2017), while lattice Boltzmann methods (LBM) provide a more nuanced representation of the interactions between hydrate distribution, sediment properties, and permeability (Hou et al., 2018). While these approaches have advanced our understanding, simplifications inherent in some models may overlook critical aspects of the dynamic interplay within porous media. This underscores the need for further refinement in numerical modeling to capture the full complexity of hydrate-bearing systems.

In addition to these efforts, theoretical models often focus on the relationship between hydrate saturation and permeability under various assumptions (Kleinberg et al., 2003; Dai and Seol, 2014; Katagiri et al., 2017); however, studies of two-phase permeability of sediments remain relatively scarce (Singh et al., 2019), representing an important area for future research. Meanwhile, advances in imaging techniques have further supported the study of hydratebearing systems. For instance, X-ray computed tomography (CT) has emerged as a powerful tool for high-precision, non-destructive imaging, extensively used to characterize hydrate microstructures and the processes of hydrate formation and dissociation (Uchida et al., 2004; Seol and Kneafsey, 2009; Lei et al., 2019; Bian et al., 2023). Moreover, CT imaging has been applied to study fluid distribution and pore structures during seepage experiments, providing valuable insights into dynamic behavior such as water displacement and fine particle migration during depressurization (Konno et al., 2013; Han et al., 2018). Despite these applications demonstrating the potential of CT imaging in capturing structural and flow dynamics, its use in characterizing the complex gas-water two-phase flow in clayey-silt reservoirs remains largely untapped.

The limited research on clayey-silt reservoirs presents an opportunity to explore the unique challenges posed by their complex structure, dynamic nature, and high water-wettability. Unlike conventional oil and gas reservoirs, disassociated hydrate reservoirs exhibit highly unconsolidated sediments, high residual water saturation, and significant capillary effects, which fundamentally alter gas—water relative permeability characteristics. These unique properties demand specialized experimental approaches beyond those commonly applied in traditional hydrocarbon-bearing formations. Bridging this knowledge gap requires integrated experimental and modeling approaches tailored to the distinct characteristics of these reservoirs. This study focuses on clayey-silt reservoirs in the Shenhu area of the South China Sea, employing gas-water two-phase flow experiments combined with highresolution X-ray CT imaging to systematically investigate the evolution of pore structure, gas-water distribution, and relative permeability characteristics under varying gas-water flow conditions. The experiments, conducted under high fluid pressures and low effective stresses, provide detailed observations of structural changes in the reservoir anticipated during prospective water flooding, particularly the behavior of gas displacing water. CT imaging is utilized to analyze pore space connectivity and the evolving distribution of residual water, while pore network modeling quantitatively evaluates evolution of the pore-throat network, revealing the formation of fracture-like pathways that enhance gasphase permeability. Furthermore, gas—water relative permeability curves are recovered to assess response of the two-phase flow region, iso-permeability point, and impacts of "water-blocking" effects. The applicability of different theoretical models for twophase flow in such sediments is also systematically evaluated, demonstrating that conventional models fail to fully capture the effects of strong capillary forces and structural alterations in these reservoirs. These findings provide novel insights into pore-scale gas-water distribution and permeability evolution, bridging the gap between experimental observations and field-scale hydrate reservoir engineering.

This study presents several key innovations in understanding gas-water two-phase flow in disassociated hydrate reservoirs. Firstly, unlike previous studies that primarily focus on synthetic hydrate-bearing sediments or numerical simulations, this work utilizes disturbed but reconstituted in-situ loose samples from a natural hydrate reservoir, providing a more realistic representation of reservoir mineralogy and hence interfacial conditions. Secondly, the novel combination of high-resolution CT imaging with concurrent two-phase flow-through experiments enables direct visualization of pore-scale structural changes and fluid distribution dynamics, offering unprecedented insights into gas displacement mechanisms. Thirdly, the application of PNM allows for a quantitative assessment of how gas injection alters pore connectivity and fracture formation, a crucial factor in enhancing gas-phase permeability. Finally, the study highlights the limitations of conventional relative permeability models in describing gas-water flow in clayey-silt sediments, underscoring the need for model improvements to account for the strong capillary effects and structural heterogeneity inherent in these reservoirs. These findings contribute to optimizing reservoir stimulation strategies by identifying key mechanisms controlling gas mobility and residual water retention, ultimately enhancing gas recovery efficiency in hydrate-bearing clayey-silt formations.

## 2. Samples

The source of the samples is a natural gas hydrate reservoir located within the Baiyun Sag of the Pearl River Mouth Basin, at a depth of approximately 1530–1545 m. The lithology of the

reservoir is clayey-silt, with an effective porosity of 33%. The pore space is filled with three phases: solid hydrates, free hydrocarbon gas, and liquid water, with a hydrate saturation of 31% (Li et al., 2018). In situ, hydrates serve as part of the load-bearing skeleton in the reservoir. When the depressurization method is applied to exploit the hydrate reservoir, the phase equilibrium of hydrates is disrupted. Solid hydrates decompose into free hydrocarbon gas and liquid water, which are extracted through the wellbore, leading to the collapse of the load-bearing skeleton composed of clayey-silt particles and solid hydrates. As the decomposition front continuously advances within the reservoir, a fully decomposed zone forms around the wellbore, where clayey-silt particles become the sole solid skeleton. This zone is highly susceptible to structural changes under stress conditions. Due to the presence of the overlying reservoir cap, the stress environment in the fully decomposed zone is determined by the pressure difference between the reservoir pressure at the decomposition front and the bottom-hole flowing pressure. Investigating the structural change mechanisms of clayey-silt particles under this pressure differential and the gas-water two-phase flow mechanisms in the fully decomposed zone is crucial. This is because the gas and water from hydrate decomposition must flow through this zone to be extracted through the production well, and the two-phase permeability of the fully decomposed zone determines the reservoir's development efficiency. Therefore, the samples used in this study are loose clayey-silt particles collected in situ from the reservoir after hydrate decomposition under necessarily low effective stresses.

To ensure the representativeness of the experimental conditions, the flow experiments are conducted under high fluid pressures and low effective stresses, simulating the stress state in the fully decomposed zone after hydrate dissociation. In actual hydrate reservoirs, the effective stress in this zone is primarily controlled by the pressure difference between the reservoir pressure at the dissociation front and the bottom-hole flowing pressure, rather than by overburden stress alone. The selection of 3 MPa/m as the experimental pressure gradient is based on both laboratory findings and field practices. In our prior study (Lu et al., 2019; Cai et al., 2020), a series of steady-state single-phase water injection tests were conducted on identical clayey-silt samples under increasing injection pressures (10-100 kPa, corresponding to 1-10 MPa/m). The results revealed that the sample permeability increased with pressure gradient up to 3 MPa/m but declined beyond this point due to compression of pores and throats, as confirmed by CT imaging. Therefore, 3 MPa/m was identified as the optimal pressure gradient that maximizes permeability while maintaining structural stability. In addition, field production data from hydrate development in the South China Sea indicate that a pressure gradient of approximately 3 MPa/m was commonly applied during production operations. This gradient is considered technically representative of actual hydrate reservoir conditions. Therefore, a 3 MPa/m gradient was adopted in this study to ensure the stability of the pore structure during two-phase flow experiments while minimizing uncertainties in relative permeability measurements due to structural alterations. The selected pressure gradient thus balances the need for realistic representation of field conditions with the requirement for maintaining stable experimental parameters, ensuring that the experimental setup accurately represents the gas-water flow behavior in the fully decomposed zone during gas production.

The mineral composition and clay content of the powdered clayey-silt samples are analyzed using a BRUKER D8 ADVANCE X-ray diffractometer. The mineral composition, in descending order of abundance, include quartz (37%), clay minerals (34%), plagioclase (13%), microcline (7%), calcite (7%), and dolomite (2%). The clay mineral compositions, also in descending order, consist of illite

(42%), illite-smectite mixed layers (21%), chlorite (20%), and kaolinite (17%), with the illite-smectite mixed layers containing ~65% illite layers. The wettability of the samples is determined using a KRÜSS goniometer by measuring contact angles. The clayey-silt samples are placed within a container submerged in a water tank and with bubbles generated by syringe, allowing them to adhere to the sample surface to form a solid—liquid—gas three-phase boundary. The Laplace—Young equation is used to fit the phase interface, and the contact angle is recovered. The measured contact angle of the clayey-silt samples is 60.3°, indicating water-wetting characteristics.

#### 3. Methods

Gas—water relative permeability is measured at successive steady states. In each step of the displacement process, gas and water are injected at a fixed flow rate ratio, and the flow continues until the outlet flow rates and differential pressure stabilize. Once stabilization is achieved, the corresponding effective permeabilities of the gas and water phases are calculated. This approach ensures that each observation is representative of steady-state conditions, distinguishing it from unsteady-state methods such as the Johnson—Bossler—Naumann method (Johnson et al., 1959), where flow rates continuously change. The steady-state nature of our method is crucial in ensuring accurate relative permeability measurements in clayey-silt samples.

The effective permeabilities of the gas and water phases are calculated using Darcy's law

$$K_{g} = \frac{2p_{0} \cdot q_{g} \cdot \mu_{g} \cdot L}{A \cdot (p_{1}^{2} - p_{2}^{2})}$$
 (1)

$$K_{W} = \frac{q_{W} \cdot \mu_{W} \cdot L}{A \cdot (p_{1} - p_{2})} \tag{2}$$

where  $q_g$  and  $q_w$  are the flow rates of gas and water, m<sup>3</sup>/s;  $\mu_g$  and  $\mu_w$ are the viscosities of gas and water, Pa·s; L is the sample length, m; A is the cross-sectional area of the sample,  $m^2$ ;  $p_1$ ,  $p_2$ , and  $p_0$ represent the inlet pressure, outlet pressure, and atmospheric pressure, respectively, Pa;  $K_g$  and  $K_g$  are the effective permeabilities of the gas and water phases, originally in SI units (m<sup>2</sup>), and are subsequently converted to millidarcies (mD) using the conversion factor 1 mD =  $9.869 \times 10^{-16}$  m<sup>2</sup>. All permeability values reported in this study are expressed in mD. Using CT scanning to obtain the gas and water saturations in the sample, the gas—water injection flow ratio is adjusted to determine the effective permeabilities of gas and water under different saturation conditions. Based on these values, the gas-water relative permeability curve for the clayey-silt sample is plotted. In addition, the CT scan images are processed to extract pore structure characteristics and analyze fluid distribution during gas—water flow. Due to the unconsolidated nature of the clayey-silt samples, mercury intrusion porosimetry could not be performed. Furthermore, nitrogen adsorption primarily characterizes nanopores, which do not significantly contribute to fluid flow in these samples. Therefore, in this study, CT imaging is the prime technique used to determine the pore structure relevant to permeability and fluid transport, providing a more accurate representation of the dominant flow pathways in the clayey-silt sediments.

## 3.1. Apparatus

The experimental apparatus primarily consists of a flow module and a CT scanning module. The flow module includes a gas source, a

water pump, a differential pressure sensor, a gas regulator, a gas flowmeter, and an electronic balance (Fig. 1). The Sanying Micro-CT scanner can non-destructively obtain high-resolution images of the sample at micro- and nano-scales. The non-magnetic holder is made of polyimide, which features high pressure resistance, strong thermal stability, and low X-ray shielding. There are two fluid inlets located at the bottom left and right sides of the holder for injecting gas and water during the experiment, while the combined gas—water outlet is positioned at the top. After passing through a gas—water separation device, the gas flow rate is measured using a gas flowmeter, and the water flow rate is obtained using an electronic balance.

#### 3.2. Procedures

The following experimental procedure is followed.

- (1) The dry clayey-silt sample is loaded into the holder, and deionized water is added to ensure the sample fully occupies the designated area of the holder (10 mm in length and 8 mm in diameter) and becomes 100% water-saturated.
- (2) Based on previous research results, to maintain the relative stability of the pore structure and absolute permeability of the clayey-silt porous medium, and to minimize uncertainties during the measurement of gas—water relative permeability curves, the displacement pressure gradient is kept below 3 MPa/m throughout the experiment. First, deionized water is injected into the sample at a constant pressure of 30 kPa using a displacement pump until the outlet flow stabilizes, ensuring structural stability. A CT scan is then performed to obtain initial state images of the sample.

- (3) The constant-pressure flow mode is switched to constantrate flow mode. A 30% KI solution is injected at a flow rate not exceeding that used during the 30 kPa water flow in the previous step. The KI solution is used to enhance the contrast of the water phase during CT scanning, facilitating the distinction between water and gas phases. KI solution is injected for several pore volumes until it completely replaces the deionized water, and a CT scan is performed.
- (4) The gas line is connected, and a small flow rate of nitrogen gas is slowly injected. Simultaneously, injection flow rate of the KI solution is reduced based on the flow rate in step 3, ensuring the differential pressure across the sample remains below 30 kPa. Once the inlet and outlet flow rates and differential pressure stabilize, the gas and water flow rates and the differential pressure are recorded, and a CT scan is conducted.
- (5) The flow rates of both the nitrogen gas and KI solution are adjusted to a fixed ratio for each measurement step. At each step, the displacement process continues until the flow rates and differential pressure reach a steady state. Only after stabilization is achieved is CT scanning performed to capture changes in pore structure and gas/water distribution. The flow rate ratio is then adjusted to the next step, and the system is again allowed to stabilize before further measurements are taken. This process is repeated until the flow rate of the KI solution reaches zero, concurrent with the maximum gas flow rate, at which point the entire experiment concludes. This stepwise approach ensures that all relative permeability measurements are conducted under steady-state conditions, distinguishing it from unsteadystate methods where flow rates change continuously during the experiment.

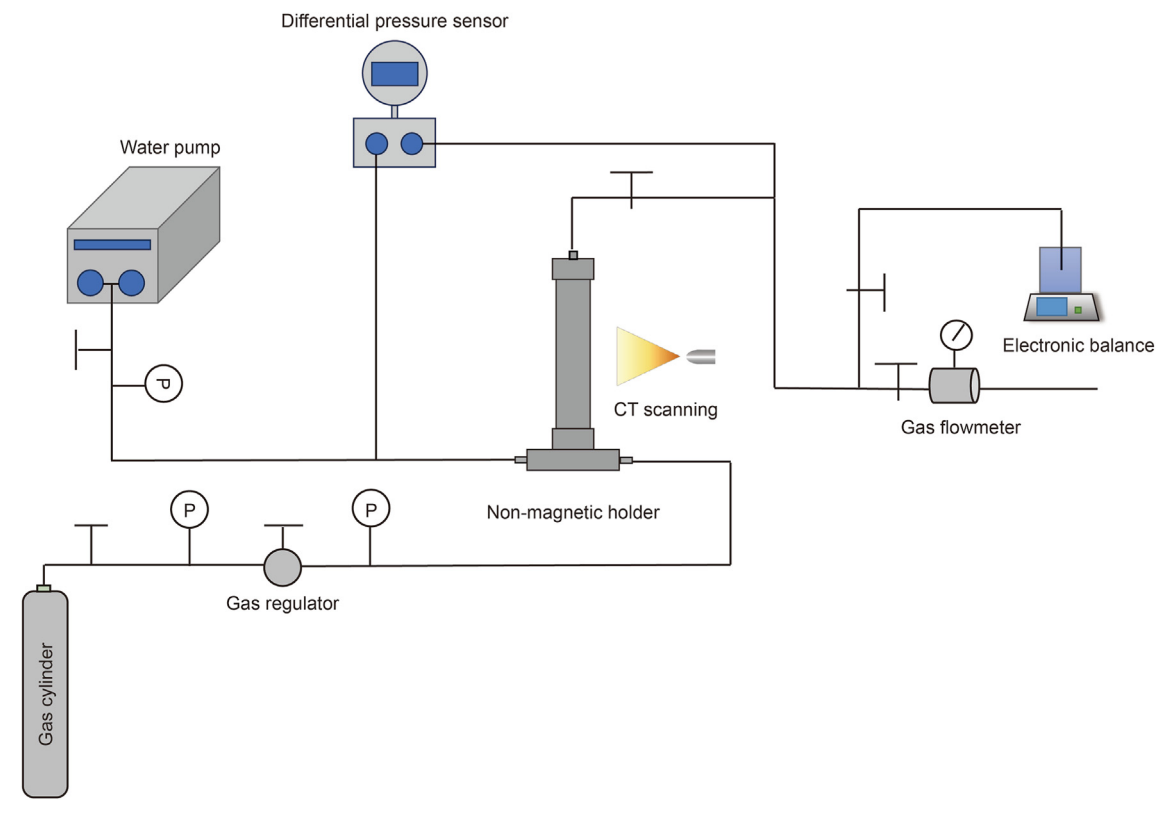


Fig. 1. Schematic of the experimental apparatus.

(6) The experimental data are processed to calculate the relative permeabilities to gas and water. The CT scan images are analyzed to determine gas and water saturations, and the gas—water relative permeability curves are plotted.

Furthermore, to ensure that the in-situ CT imaging is completed without disrupting the steady-state displacement process, the following procedure is adopted. During each experimental step, the gas and water flow rates are adjusted to a fixed ratio and maintained until the outlet flow rates and differential pressure stabilized, ensuring steady-state conditions. Once steady-state is reached, both the inlet and outlet valves of the sample holder are temporarily closed to isolate the system and maintain the internal gas—water distribution static. Then, the CT scanning process, which lasted several hours, was then performed under these stabilized conditions to capture high-resolution images of the pore structure and fluid distribution. After scanning, the inlet and outlet valves are reopened to resume the displacement experiment without affecting the ongoing steady-state flow process. This approach ensured that the CT imaging provided a true representation of the in-situ gas-water distribution during steady-state flow, without introducing artifacts due to fluid redistribution during scanning.

### 4. Results and discussion

#### 4.1. Gas—water flow rate and relative permeability

At the beginning of the experiment, a differential pressure of 30 kPa is applied to stabilize the structure of the clavey-silt sample. Once the flow rate stabilizes, the water-phase effective permeability is calculated using Eq. (2) and is found to be 8.600 mD, which aligns well with the CT-derived pore structure observations. According to permeability classification, the clayey-silt sample belongs to a low-permeability reservoir. The flow mode is then switched from constant-pressure to constant-rate to prepare for the subsequent injection of two-phase fluids under constant flow conditions. To ensure that the differential pressure does not exceed 30 kPa during gas injection, which helps maintain the structural integrity of the sample and avoids changes to the absolute permeability that could affect the relative permeability curve, the water flow rate is first reduced to half of that in Stage 1. The calculated water effective permeability remains consistent with that of Stage 1, indicating that the structure of the clayey-silt sample stabilizes after the 30 kPa flow process.

In Stage 3, the water flow rate is further reduced slightly, and the gas flow rate is set to the lowest value controllable by the apparatus. Gas-water two-phase displacement begins, and once the outlet gas and water flow rates stabilize, the effective permeabilities of both phases are calculated. At this point, the effective permeability of the water phase is approximately 27 times that of the gas phase. In the subsequent stages (Stages 4 and 5), the water flow rate is further reduced while the gas flow rate is increased. By Stage 5, the water flow rate reaches the lowest limit controllable by the apparatus. From this stage onward, the water flow rate remains constant while the gas flow rate is gradually increased. In Stage 5, the effective permeabilities of water and gas phases become nearly equal, representing the intersection point on the relative permeability curve. The gas flow rate is continuously increased in the following stages, and by Stage 8, the effective permeability of the gas phase reaches approximately 19 times that of the water phase. Finally, in Stage 9, the gas flow rate remains constant while the water injection is stopped. Once the outlet gas flow rate stabilizes, the gas permeability is calculated. At this point, the gas permeability reaches the maximum value observed throughout the experiment. The relative permeabilities of water and gas phases at

each experimental stage are obtained by dividing their respective effective permeabilities by this maximum gas permeability.

### 4.2. Sample structure and gas—water distribution

The 2D CT cross-sectional images obtained during the gas—water two-phase experiments (from experimental stages marked with an asterisk in Table 1, with a scanning resolution of 3.69  $\mu m$  and pixel dimensions of  $1300\times1300\times750$ ) are shown in Figs. 2 and 3. From the water saturation images of Stage 1, it can be observed that the clayey-silt sample contains two distinct particle sizes. Based on the particle shapes and previous QEMSCAN experiments (Lu et al., 2022), the larger irregular particles are primarily composed of quartz, while the smaller particles are mainly clay minerals. This difference in particle sizes results in varying pore sizes within the sample, including large pores distributed between quartz particles, smaller pores distributed between clay minerals, and larger foraminiferal pores (indicated by white ring-like features around the pores in the images).

In Stage 2, after marking the water in the sample with KI solution, it is observed that most of the sample's pores are fully saturated with the solution, with only a small portion of pores remaining unsaturated, possibly due to connectivity issues. In Stage 3, as gas injection begins, the solution in the lower-right pores of the XY plane slice is displaced, and the pores expand and extend to form clearly connected fracture-type pores. This observation aligns with the general understanding of seepage behavior in clayey-silt samples. Specifically, during single-phase water injection through clayey-silt samples, liquid flows through the sample's pores while the structure remains relatively stable. When single-phase water injection pressure increases, the sample undergoes overall structural creep (Lu et al., 2019; Cai et al., 2020). However, during gas injection, due to the high capillary pressure in clayey-silt samples (Xia et al., 2023), the gas displacement pressure, even if unable to exceed capillary pressure, can exceed the structural stability pressure of the sample, forming seepage channels for gas flow (Xia et al., 2024). These channels appear as connected fracture-like pores. The capillary pressure within these fractures is relatively low, allowing gas to quickly displace fluids from the pores and form preferential gas flow pathways. Subsequently, as the gas injection rate increases and the water injection rate decreases (Stages 5, 7, and 9), the already-formed fracture-type gas flow channels enable only a small portion of water in the smaller pores to be further displaced, and no new fracture-type gas flow channels are formed.

#### 4.3. Gas—water saturation and heterogeneous distribution

Since this experiment involves in-situ scanning of the sample during the process, the reconstructed data volumes are processed through image cropping, alignment, smoothing, and region selection. This allows for a precise comparison of the spatial positions of pores and particles across different data volumes. The image differencing method is then employed to obtain the pore space and fluid seepage space. The injected 30% KI solution, containing iodine with a high atomic number, appears bright in the CT scan due to its high grayscale values, while the gas-phase regions, which lack a contrast agent, appear dark. By utilizing the grayscale differences between the water and gas phases, the grayscale data can be segmented to identify the original pore space and the gas-phase distribution under gas-water displacement conditions (Fig. 4). A comparison between the pore structure in Stage 1 and the gasphase distribution in Stage 3 reveals that at a low gas flow rate, the gas initially displaces liquid from the larger, connected pores within the sample. As the gas displacement pressure gradually increases, the liquid in smaller pores is progressively displaced.

**Table 1**Water and gas flow rates and permeabilities under different up- and down-stream pressures.

Stag	e Differential pressure, kPa	Water flow rate, mL/min	Gas flow rate, mL/min	Water-phase effective permeability, mD	Gas-phase effective permeability, mD	Water-phase relative permeability	Gas-phase relative permeability
1ª	30.000	0.120	0.000	8.600	0.000	0.422	0.000
$2^{a}$	16.000	0.065	0.000	8.680	0.000	0.426	0.000
3 <sup>a</sup>	25.500	0.042	0.100	3.500	0.132	0.172	0.006
4	16.000	0.022	0.300	2.890	0.657	0.142	0.032
5 <sup>a</sup>	13.000	0.008	0.500	1.270	1.366	0.062	0.067
6	14.500	0.008	1.000	1.140	2.433	0.056	0.119
7 <sup>a</sup>	14.000	0.008	4.000	1.180	10.101	0.058	0.495
8	17.500	0.008	9.000	0.950	17.893	0.046	0.878
9 <sup>a</sup>	15.500	0.000	9.000	0.000	20.387	0.000	1.000

#### Note:

<sup>&</sup>lt;sup>a</sup> Indicates that CT scanning is performed during this stage of the experiment.

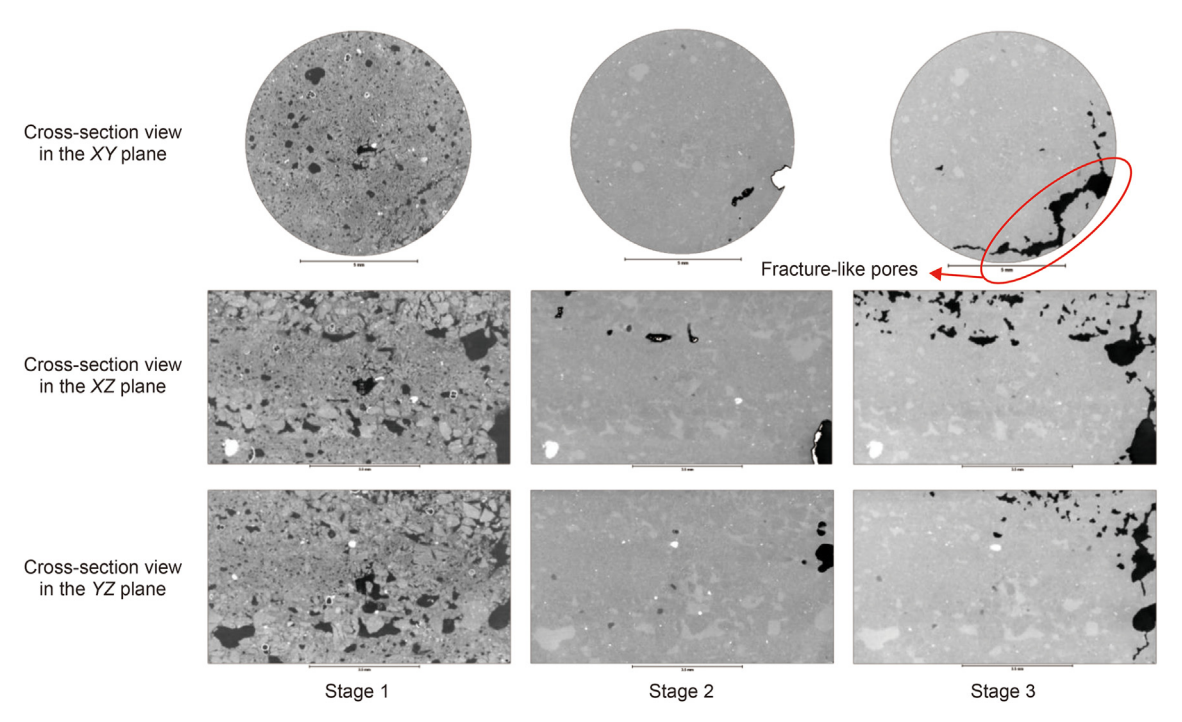


Fig. 2. Cross-sectional images from three angles for Stages 1–3.

However, by the end of the displacement process, a certain amount of fluid in the smaller pores remains undisturbed.

Based on the pore space data and gas—water phase distribution data at different experimental stages, the total porosity of the sample is calculated as 0.207 by determining the proportion of pore voxels to the total rock voxels in Stage 1. The gas and water phase proportions in the subsequent stages are used to determine the gas—water saturations under different conditions (Table 2). The gas and water saturations in Stage 2 indicate that the initial water saturation of the sample is relatively high, approximately 90%. With the onset of gas injection in Stage 3, the gas saturation shows a significant increase, while the water saturation decreases notably. This represents the most substantial change in gas saturation among all the gas displacement stages. As gas injection continues, even with a several-fold increase in gas flow rate, the change in saturation becomes smaller. Ultimately, approximately 56% of the water remains in the sample, indicating a relatively high residual water saturation.

Pore volume fraction and gas-phase volume fraction in 2D slices in the  $\it Z$  direction at different stages are plotted as a curve (Fig. 5). From the curve of Stage 1, it can be observed that the pore space

exhibits significant heterogeneity in the *Z* direction, with two prominent peaks appearing between slice 100 and slice 200 and after slice 600. This heterogeneity in the pore space distribution also affects the subsequent displacement process. Stage 2 represents the gas-phase distribution under water-saturated conditions, which corresponds to the residual gas distribution. It can be seen that a significant portion of the space between slice 100 and slice 200 remains unsaturated with water, while the peak pores after slice 600 are better saturated. This heterogeneity in saturation distribution is likely caused by differences in pore connectivity. The subsequent gas-phase displacement (Stages 3, 5, 7, and 9) reveals that the water within the 100–200 peak is nearly displaced by Stage 5, whereas water in the pores beyond slice 600 continues to be displaced up to Stage 9.

These observations together indicate that both pore heterogeneity and connectivity influence the displacement process. The heterogeneity in pore distribution results in two peaks, which contain a significant amount of gas and water phases. Differences in the connectivity of these two peak regions (based on saturation and displacement conditions) suggest that the pores beyond slice 600 have better connectivity compared to those between slice 100 and

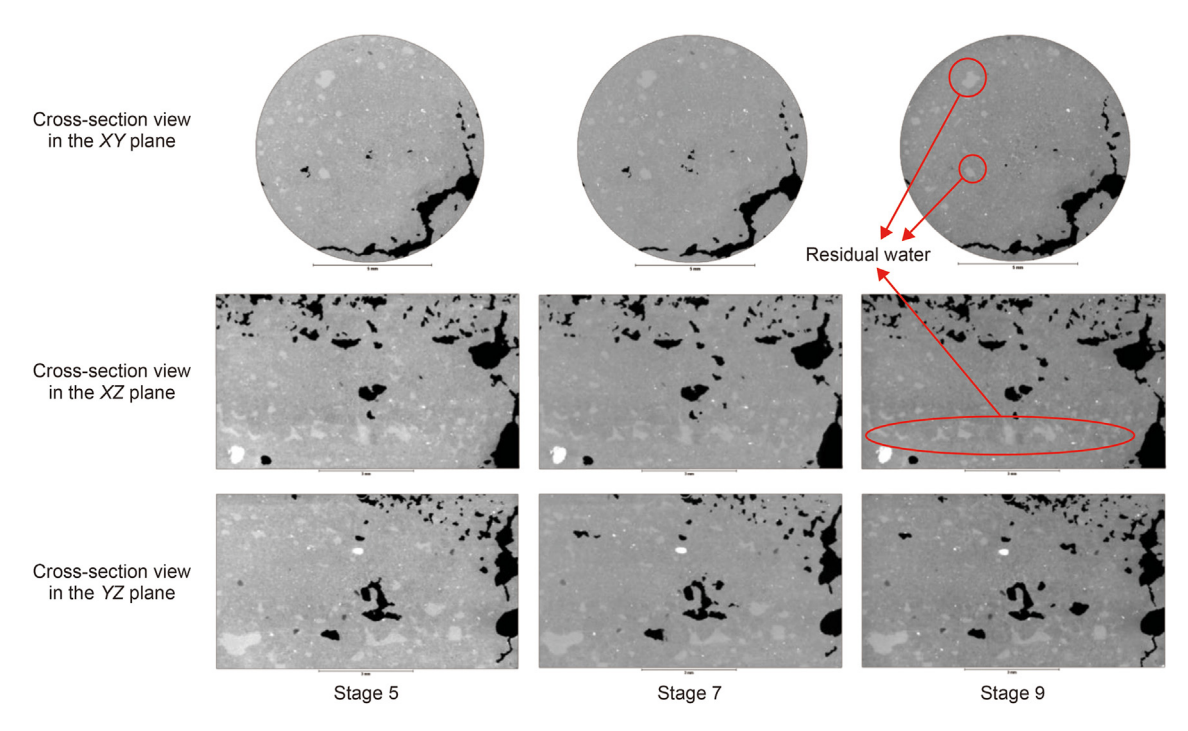


Fig. 3. Cross-sectional images from three angles for Stages 5, 7, and 9.

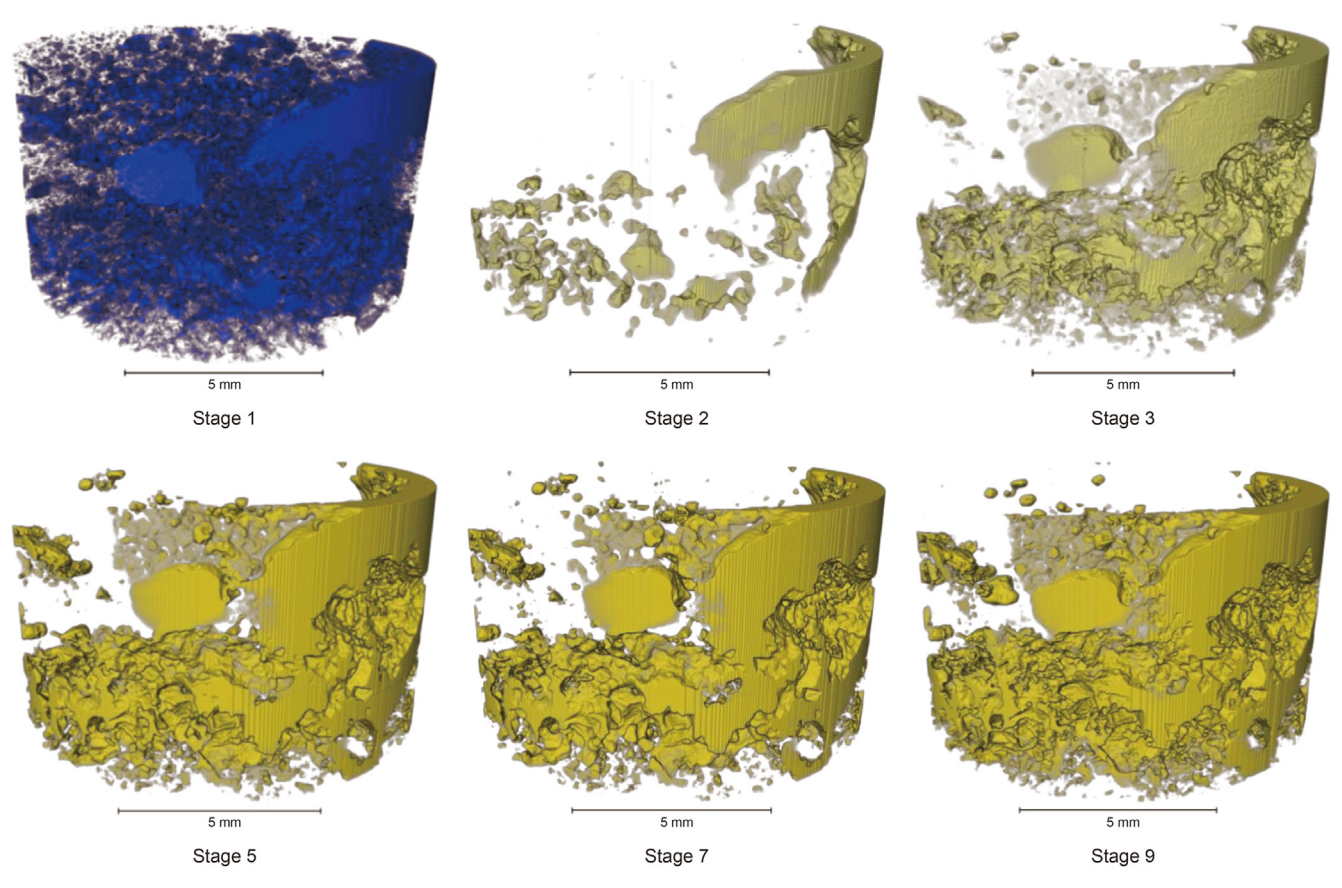


Fig. 4. 3D structure of the sample during the gas—water displacement (blue represents the pore space in Stage 1, while yellow represents the gas-phase space in the other stages).

slice 200. As a result, less gas-phase space remains unsaturated during the water saturation process (Stage 2), and more gas-phase space grows during subsequent displacement (Stage 9). This

demonstrates that pore heterogeneity and connectivity jointly influence the entire gas—water displacement process.

**Table 2**Changes in gas—water saturation within the sample pores during the gas—water displacement process.

Phase	Gas		Water		
Parameter	Volume fraction	Saturation	Volume fraction	Saturation	
Stage 2	0.028	0.137	0.179	0.863	
Stage 3	0.068	0.330	0.139	0.670	
Stage 5	0.081	0.391	0.126	0.609	
Stage 7	0.083	0.400	0.124	0.600	
Stage 9	0.091	0.439	0.116	0.561	

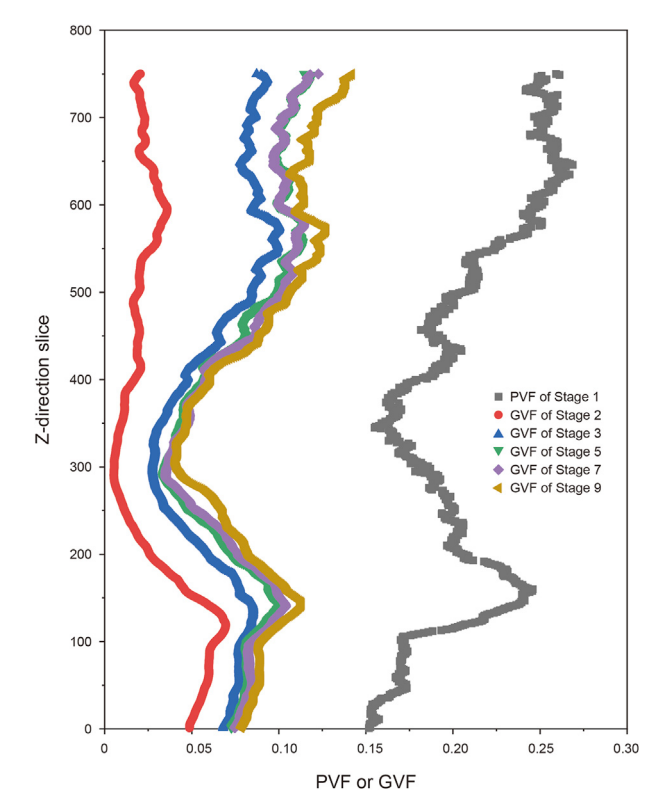


**Fig. 5.** Pore volume fraction (PVF) of Stage 1 and gas-phase volume fraction (GVF) of Stages 2, 3, 5, 7, and 9 in 2D slices along the Z direction.

#### 4.4. Pore network model for gas-phase space

The pore and gas-phase spaces at different experimental stages are modeled using the pore network modeling method (Dong and Blunt, 2009; Blunt et al., 2013), as shown in Fig. 6. Comparing Stage 1 and Stage 2, it is evident that the saturation process is effective, with only some edge pores and isolated small pores remaining unsaturated with water. Once gas injection begins, the pore-throat network for gas flow is established as early as Stage 3. Subsequent gas injection primarily expands this existing pore-throat network, displacing water from the surrounding throats and increasing the gas-phase space, which enhances permeability. Comparing Stage 1 and Stage 9, it is observed that by the end of displacement, a certain amount of water remains trapped in smaller pores, while the pore and throat sizes exhibit some degree of enlargement after gas injection.

From the pore network model, the pore-throat radius distribution of the pore space and gas-phase space during the displacement process (Figs. 7 and 8) and the pore-throat parameters (Table 3) can be directly obtained. As shown in Figs. 7(b) and 8(b), in Stage 2, the pore-throat space unsaturated with water is relatively evenly

distributed. However, starting from Stage 3 with gas injection, the pore-throat distribution becomes noticeably heterogeneous. Peaks appear at 100  $\mu m$  for pores and at 70–80  $\mu m$  for throats. These small pores and throats, which are abundant, serve as the primary seepage space for the gas phase and play a critical role in pore connectivity. Comparing the pore-throat volume distributions in Stage 1 (Figs. 7(a) and 8(a)), it is observed that water is difficult to be displaced from pores with peak radii around 60  $\mu m$  and throats with peak radii around 30  $\mu m$ . These pores and throats are the primary storage space for residual water. Additionally, several new peaks appear at larger radii (pores larger than 300  $\mu m$  and throats larger than 200  $\mu m$ ). These larger pores and throats correspond to the fracture spaces observed after gas displacement in Figs. 2 and 3, which become the dominant flow pathways for the gas phase.

By examining the pore-throat parameters during the gas displacement process in Stage 3, 5, 7, and 9 in Tables 3 and it is observed that the average pore radius, average throat radius, and average throat length reach their maximum values at the beginning of gas displacement (Stage 3). As the displacement progresses and the gas flow rate increases, these average values gradually decrease, indicating that the later stages primarily involve the displacement of water in smaller pores and throats, which reduces the averages. The maximum pore radius, maximum throat radius, and maximum throat length remain relatively unchanged after Stage 5, suggesting that water in the largest pores and throats is displaced during the early stages of displacement. The coordination number, which reflects the connectivity of the pore-throat network, decreases progressively from Stage 3 to Stage 7. This is because water in more isolated and edge-connected pores is displaced, reducing overall connectivity. By Stage 9, the coordination number had increased again, indicating that water had been displaced from many small throats, improving the overall connectivity of the gas-phase space. Comparing the post-displacement parameters with the original pore-throat parameters from Stage 1, it is evident that the average pore radius, average throat radius, and average throat length in Stage 1 are significantly smaller than those in Stage 9. This indicates that a substantial amount of water remains trapped in small pores and throats, which do not participate in gas flow. The maximum pore radius, maximum throat radius, and maximum throat length in Stage 1 are smaller than those in Stage 9, suggesting that the gas displacement process leads to structural changes, with the formation of new fractures.

To clarify the connection between pore-throat parameters and relative permeability behavior, we emphasize the role of structural evolution during gas injection. As shown in Table 3, increases in average and maximum pore/throat radii correspond to enhanced gas-phase permeability, due to the formation of large, fracture-like pores that serve as preferential flow channels. In contrast, the persistence of small pores and throats contribute to high residual water saturation, as water remains trapped in these low-connectivity regions.

The coordination number offers additional insight into connectivity: higher values indicate a more connected pore-throat network, which facilitates continuous gas pathways and improves gas-phase permeability. As the coordination number increases in the later displacement stages (e.g., Stage 9), gas flows more effectively, while water-phase permeability decreases due to disconnection of water pathways.

These trends directly support the shape and shift of the relative permeability curves in Section 4.5. Specifically, the right-shifted iso-permeability point and narrow two-phase flow region are manifestations of capillary barriers created by pore-scale heterogeneity, with pore-throat geometry playing a decisive role in controlling two-phase flow dynamics. Therefore, the evolution of pore-throat parameters during displacement provides a mechanistic

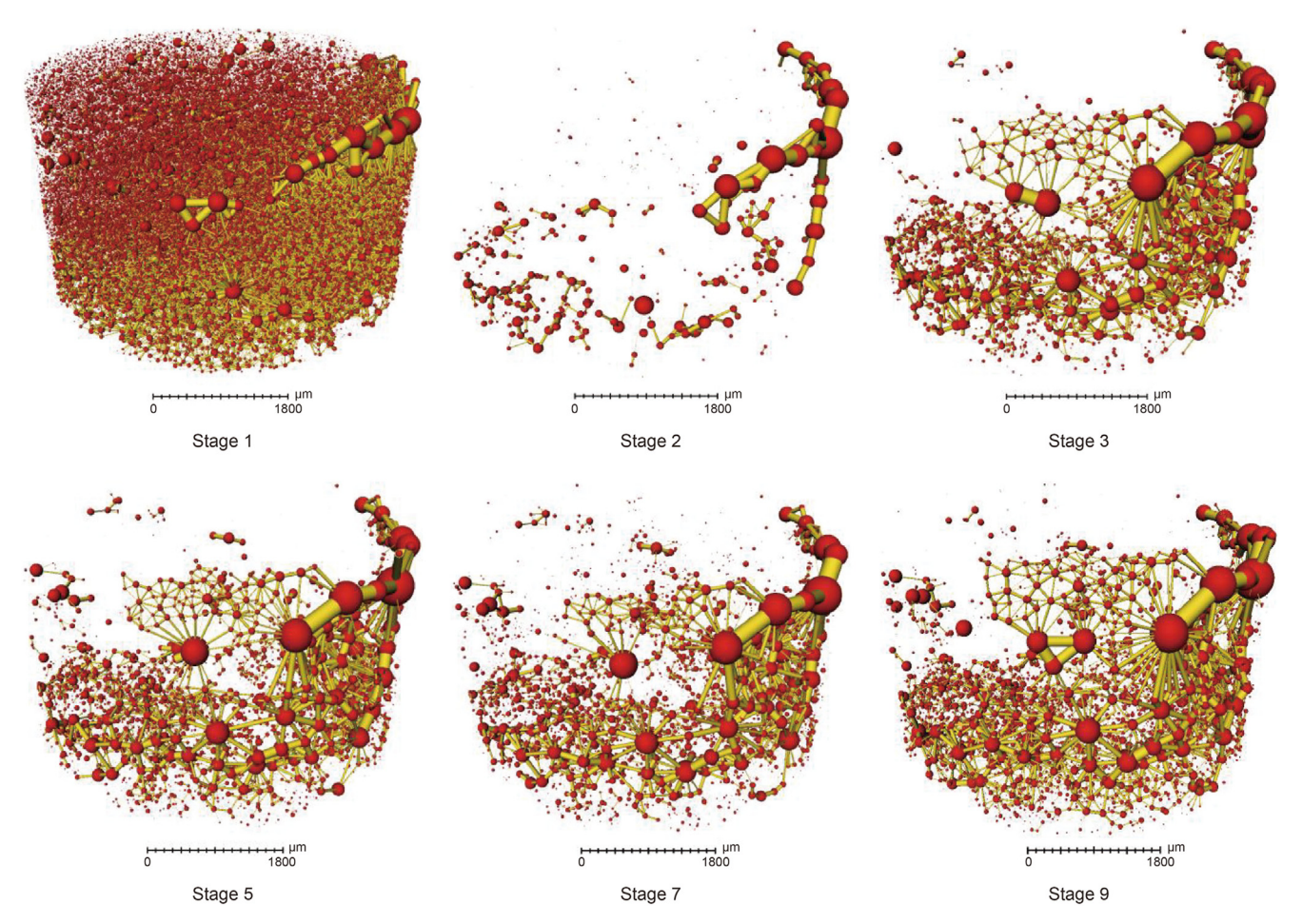


Fig. 6. Pore network models at different experimental stages (red represents pores, yellow represents throats).

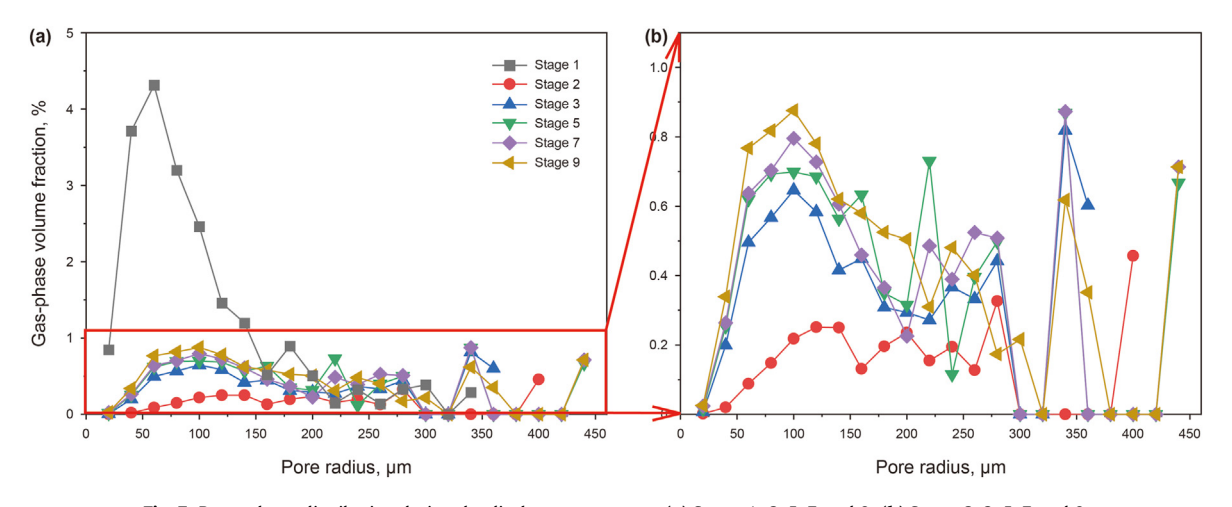


Fig. 7. Pore volume distribution during the displacement process. (a) Stages 1–3, 5, 7, and 9; (b) Stages 2, 3, 5, 7, and 9.

explanation for the relative permeability behavior observed in dissociating clayey-silt hydrate reservoirs.

## 4.5. Gas-water relative permeability curves

The relative permeability curves, plotted using the gas-phase relative permeability data from Table 1 and the gas and water saturations from Table 2, are shown in Fig. 9. The curves reveal that

during the initial stage of gas—water two-phase flow, as gas injection increases and water injection decreases, the water saturation decreases while the gas saturation increases on the right side of the iso-permeability point. This leads to a continuous increase in gas-phase pore space, allowing the gas phase to gradually form a continuous phase. As a result, the gas permeability increases slowly, while the water-phase flow capacity declines rapidly. On the left side of the iso-permeability point, as the gas saturation further

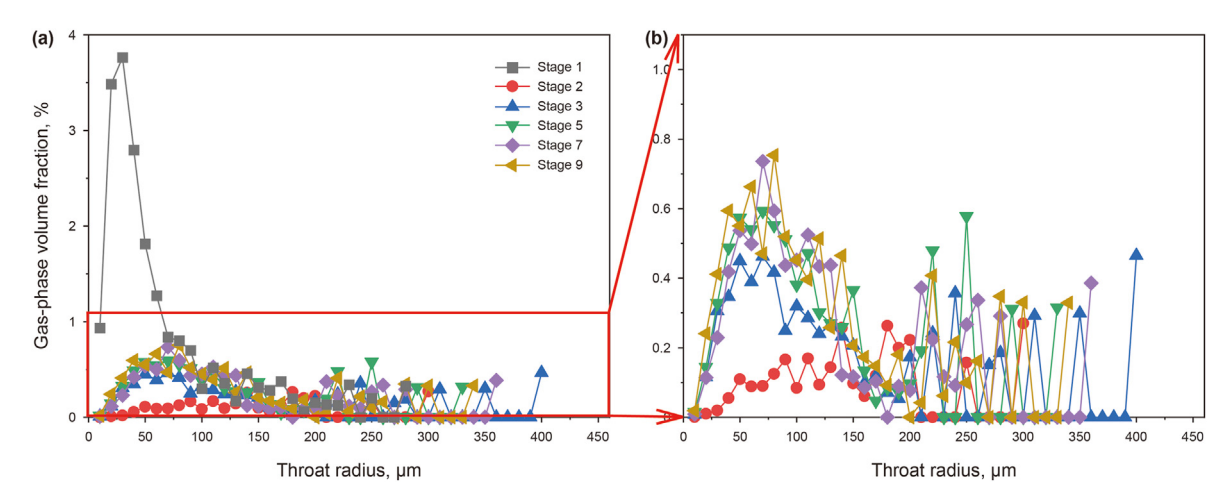


Fig. 8. Throat volume distribution during the displacement process. (a) Stages 1-3, 5, 7, and 9; (b) Stages 2, 3, 5, 7, and 9.

**Table 3**Pore-throat parameters of the gas-phase space during the displacement process.

Stage	e Average pore radius, μm	Maximum pore radius, μm	Average throat radius, $\mu m$	Maximum throat radius, μm	Average throat length, $\mu m$	Maximum throat length, μm	Coordination number
1	10.370	324.222	9.764	276.082	72.949	744.693	0.977
2	38.137	380.887	57.242	293,414	232.789	899.338	0.787
3	44.166	350.017	33.699	394.175	192.825	1124.220	1.939
5	36.268	430.320	31.359	323.822	176.300	1200.280	1.604
7	32.504	439.275	33.618	353.393	174.235	1198.110	1.146
9	32.761	439.639	28.702	333.583	171.085	1183.630	1.549

increases, the gas permeability rises rapidly, causing a slower decline in water-phase permeability, eventually reaching a state of residual water saturation.

Compared to conventional relative permeability curves, the small pores in the clayey-silt samples exhibit a stronger water retention capacity, resulting in a narrower two-phase flow region, a lower iso-permeability point, and higher residual water saturation. When the gas phase enters the pores, it must overcome significant capillary forces and tends to flow preferentially through larger pore channels, forming dominant gas flow pathways. This behavior makes it difficult for gas and water to flow simultaneously within the same pores. The narrow two-phase flow region, low iso-permeability point, and rightward shift indicate poor sorting of the pore space and strong hydrophilicity of the medium. Additionally, the rapid decline in gas permeability with increasing water saturation highlights a strong "water-blocking" effect, where the water-phase flow capacity is significantly reduced due to the strong water retention forces within the clayey-silt pores.

In practical development, if the water phase within the clayey-silt porous medium cannot be efficiently displaced by gas released from hydrate decomposition, gas-phase flow will be severely restricted in water-filled pores. Therefore, to efficiently develop the gas produced from hydrate decomposition, it is necessary to implement secondary modification of the clayey-silt porous medium within the hydrate decomposition zone. This modification aims to effectively expand the two-phase flow space, creating favorable flow pathways for gas, and enabling stable gas production.

Although only one set of CT-scanning-derived relative permeability is presented in this paper, two additional steady-state gas—water displacement experiments were conducted on similar clayey-silt samples to evaluate repeatability. The resulting relative permeability curves from those tests exhibited consistent shapes and trends, including the narrow two-phase flow region, the right-

shifted iso-permeability point, and the strong "water-blocking" effect, confirming the reproducibility of the experimental observations. However, these auxiliary experiments were conducted without CT scanning due to the limited availability of scanning-time prompted by expense. As a result, water saturation and pore structure evolution could not be obtained for those runs, and thus they are not included in the main analysis. Nevertheless, the current dataset is representative and sufficient for characterizing the gas—water flow behavior in clayey-silt hydrate reservoirs.

Furthermore, the relative permeability models fitted in Section 4.6 are not intended for predictive modeling but rather to help visualize and describe the general behavior and trends of the measured relative permeability data. Despite limited data points, the fitting serves to highlight key features such as strong capillary control and structural evolution, and to compare the performance of different fitting models for clayey-silt reservoirs.

# 4.6. Gas-water relative permeability models

In theoretical models explaining the variation of two-phase relative permeability with saturation, the Brooks–Corey (BC) model and van Genuchten (VG) model are commonly used. The relationships between water-phase relative permeability, gasphase relative permeability, and saturation follow the BC equation (Brooks, 1965):

$$k_{\mathsf{rW}} = \left(S_{\mathsf{W}}^*\right)^{3+2/\lambda} \tag{3}$$

$$k_{\rm rg} = (1 - S_{\rm w}^*)^2 \left[ 1 - (S_{\rm w}^*)^{1+2/\lambda} \right]$$
 (4)

where  $k_{\rm rw}$  and  $k_{\rm rg}$  are the relative permeabilities of water and gas phases, dimensionless;  $\lambda$  is the index of pore-size distribution,

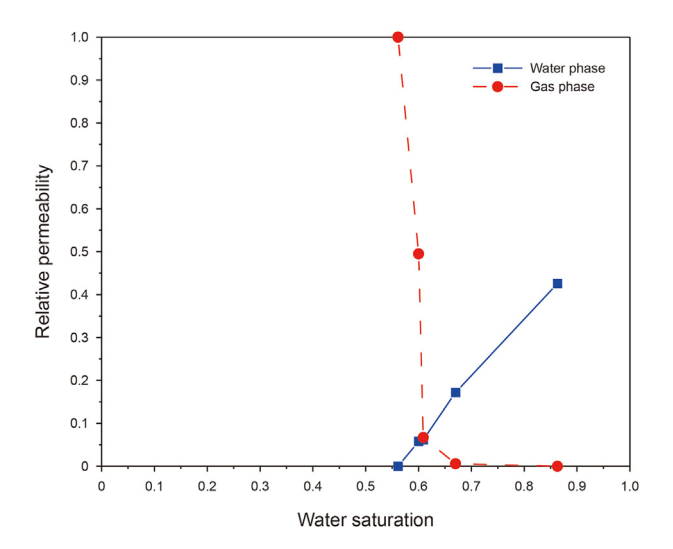


Fig. 9. Relative permeability curves.

dimensionless; and  $S_w^*$  is the effective saturation, dimensionless, calculated using the following equation:

$$S_{W}^{*} = \frac{S_{W} - S_{Wr}}{1 - S_{Wr} - S_{nWr}}$$
 (5)

where  $S_{\text{wr}}$  represents the residual water saturation, which is 0.561; and  $S_{\text{nwr}}$  represents the irreducible gas saturation, which is 0.137.

The VG model for gas—water two-phase relative permeability is expressed as follows (van Genuchten, 1980; Lenhard and Parker, 1987; Parker et al., 1987):

$$k_{\text{rw}} = (S_{\text{w}}^*)^{1/2} \left[ 1 - \left( 1 - (S_{\text{w}}^*)^{1/m} \right)^m \right]^2$$
 (6)

$$k_{\rm rg} = (1 - S_{\rm w}^*)^{1/2} \left[ 1 - (S_{\rm w}^*)^{1/m} \right]^{2m}$$
 (7)

where m is the shape factor, reflecting the characteristics of the pore size distribution, dimensionless.

The results obtained by simultaneously fitting the gas—water two-phase experimental data using the BC and VG models are

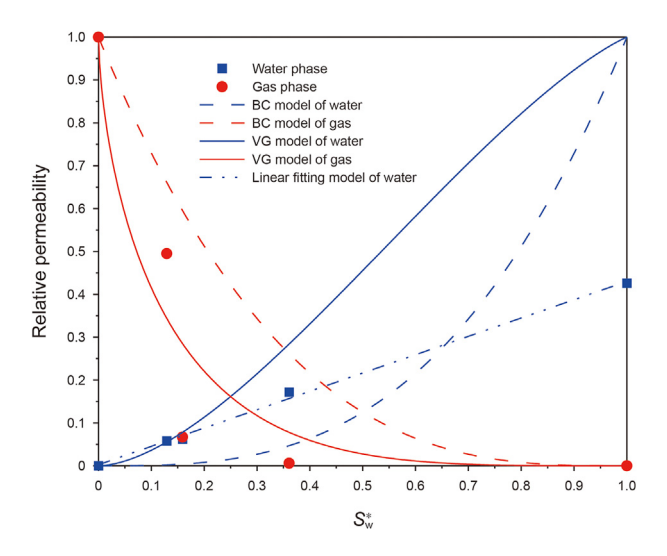


Fig. 10. Relative permeability models.

shown in Fig. 10. The VG model demonstrates an excellent fit to the gas-phase relative permeability data, with a correlation coefficient reaching 0.900. This indicates that the VG model can effectively characterize the variation of gas-phase relative permeability with saturation for clayey-silt samples. Interestingly, in this fitting, the m value exceeds 1, which contradicts the theoretical range of VG (m is expected to range from 0 to 1). This discrepancy is likely due to structural changes in the clayey-silt samples during the permeability experiments (Figs. 2 and 3). Unlike the phenomena observed in this experiment, conventional soils typically exhibit relatively stable structures during permeability testing, resulting in insignificant variations in the m value. The BC model shows a relatively poor fit to the gas-phase relative permeability data, with a correlation coefficient of only 0.509.

However, the VG and BC models both perform poorly in fitting the water-phase data. The VG model aligns reasonably well with the experimental data trend at lower effective water saturations but significantly overestimates the water-phase permeability at higher saturations. Conversely, the BC model underestimates the water-phase permeability at lower saturations and overestimates it at higher saturations. The poor fitting performance of these models may be attributed to the complex pore distribution of the clayey-silt samples and the pronounced "water-blocking" effect. Additionally, it is observed that a linear fitting relationship better explains the correlation between water-phase relative permeability and saturation for clayey-silt samples, with a correlation coefficient as high as 0.997.

$$k_{\text{TW}} = 0.4275S_{\text{W}}^* + 0.0026 \tag{8}$$

#### 5. Conclusions

This study investigates gas—water two-phase flow experiments using clayey-silt reservoir samples from the Shenhu area of the South China Sea. CT scanning technology is employed to observe structural changes and gas—water distribution under different flow rates. The pore structure characteristics, saturation distribution, and their effects on gas—water relative permeability are analyzed. The main conclusions are as follows:

- (1) During the gas—water two-phase displacement experiments, significant changes in permeability are observed by gradually adjusting the gas and water flow rates. As the gas flow rate increases and the water flow rate decreases, fracture-type flow channels gradually form in the sample. Gas-phase permeability increases significantly and stabilizes, ultimately reaching 19 times that of water-phase permeability.
- (2) CT scanning reveals significant heterogeneity in the pore distribution of the sample. Gas preferentially displaces water from larger pores, followed by gradual displacement from smaller pores, but approximately 56% of the water remains as residual water that cannot be displaced. The formation of fractures significantly enhances gas-phase connectivity, while the high residual water saturation reflects the strong water retention capacity of the clayey-silt reservoir.
- (3) The pore network analysis shows that gas injection establishes and expands a pore-throat network, displacing water and enhancing connectivity. Fracture-like pores form during gas flow, increasing the maximum pore and throat radii, while residual water remains trapped in smaller pores and throats. The coordination number initially decreases due to water displacement in edge-connected pores but improves in later stages as smaller throats contribute to connectivity.

These structural changes highlight the influence of pore heterogeneity and connectivity on gas—water flow behavior in clayey-silt samples.

- (4) The gas—water relative permeability curves show a narrow two-phase flow region and a rightward-shifted iso-permeability point, indicating high capillary forces and poor sorting of the flow space in clayey-silt reservoirs. Gas-phase permeability increases significantly with the formation of fracture-like pores, which act as preferential flow channels. In contrast, water-phase permeability declines rapidly due to the "water-blocking" effect and eventually stabilizes at residual water saturation.
- (5) The van Genuchten (VG) model fits the gas-phase relative permeability well (correlation coefficient 0.900) but performs poorly for the water-phase data. The Brooks-Corey (BC) model shows poor fitting for both gas and water phases, while linear fitting provides a more accurate representation of water-phase relative permeability (correlation coefficient 0.997). This likely results from dynamic changes in structure driven by the high internal fluid pressures and low applied total stresses.

In conclusion, the high clay content, hydrophilicity, and fracture formation characteristics of clayey-silt reservoirs play a critical role in influencing gas-water relative permeability and overall gas production efficiency. This study provides a comprehensive porescale investigation into gas-water flow in disassociated hydrate reservoirs, highlighting key mechanisms affecting gas permeability and residual water retention in clayey-silt sediments. By integrating high-resolution CT imaging, pore network modeling, and relative permeability analysis, this research offers new insights into the structural evolution and transport dynamics of such reservoirs. The findings emphasize that optimizing reservoir stimulation techniques, such as enhancing fracture connectivity and minimizing residual water saturation, is essential to promote the development of fracture flow channels, improve gas flow pathways, and enhance overall reservoir performance. These advancements bridge the gap between experimental observations and field-scale reservoir behavior, offering valuable guidance for the optimization of gas production strategies and the future development of hydrate reservoirs.

The findings of this study provide direct implications for improving hydrate reservoir engineering practices. Unlike conventional oil and gas reservoirs, disassociated hydrate reservoirs exhibit high clay content, strong water-wettability, and are unconsolidated, which significantly influences gas-water relative permeability and overall gas recovery efficiency. This study demonstrates that capillary forces and structural heterogeneity play dominant roles in controlling gas—water transport, requiring novel modeling approaches and customized development strategies for efficient gas extraction. First, the identification of fracture-like pores as primary gas flow pathways suggests that reservoir stimulation techniques, such as hydraulic fracturing or chemical stimulation, could be optimized to enhance fracture connectivity and minimize residual water saturation. Second, the characterization of relative permeability curves highlights the necessity of controlling production pressures to mitigate "water-blocking" effects and sustain gas mobility. Finally, pore network modeling results indicate that monitoring changes in pore connectivity during production can help predict permeability evolution, informing real-time reservoir management strategies. These insights contribute to developing more effective and sustainable natural gas hydrate production techniques, bridging the gap between fundamental pore-scale observations and large-scale reservoir exploitation.

#### **CRediT authorship contribution statement**

**Yu-Xuan Xia:** Writing — original draft, Methodology, Funding acquisition, Formal analysis, Data curation. **Derek Elsworth:** Writing — review & editing, Methodology, Formal analysis. **Sai Xu:** Formal analysis, Data curation. **Xuan-Zhe Xia:** Methodology, Formal analysis. **Jian-Chao Cai:** Writing — review & editing, Supervision, Methodology, Funding acquisition, Conceptualization. **Cheng Lu:** Validation, Resources, Methodology, Funding acquisition.

#### **Declaration of competing interest**

The authors declare that they have no known competing financial interests or personal relationships that could have appeared to influence the work reported in this paper.

#### Acknowledgements

The authors are grateful to the National Natural Science Foundation of China (Nos. 42302143, 42172159) and China Geological Survey Project (No. DD20211350). Derek Elsworth gratefully acknowledges support from the G. Albert Shoemaker endowment.

#### References

- Ahn, T., Lee, J., Huh, D.-G., Kang, J.M., 2005. Experimental study on two-phase flow in artificial hydrate-bearing sediments. Geosystem Eng. 8 (4), 101–104. https://doi.org/10.1080/12269328.2005.10541244.
- Ai, L., Zhao, J., Wang, J., Song, Y., 2017. Analyzing permeability of the irregular porous media containing methane hydrate using pore network model combined with CT. Energy Proc. 105, 4802–4807. https://doi.org/10.1016/j.egypro.2017.03.950.
- Bian, H., Qin, X., Sun, J., Luo, W., Lu, C., Zhu, J., Ma, C., Zhou, Y., 2023. The impact of mineral compositions on hydrate morphology evolution and phase transition hysteresis in natural clayey silts. Energy 274, 127303. https://doi.org/10.1016/ j.energy.2023.127303.
- Blunt, M.J., Bijeljic, B., Dong, H., Gharbi, O., Iglauer, S., Mostaghimi, P., Paluszny, A., Pentland, C., 2013. Pore-scale imaging and modelling. Adv. Water Resour. 51, 197–216. https://doi.org/10.1016/j.advwatres.2012.03.003.
- Brooks, R.H., 1965. Hydraulic Properties of Porous Media. Colorado State University. Cai, J., Xia, Y., Lu, C., Bian, H., Zou, S., 2020. Creeping microstructure and fractal permeability model of natural gas hydrate reservoir. Mar. Petrol. Geol. 115, 104282. https://doi.org/10.1016/j.marpetgeo.2020.104282.
- Chen, C., Zhang, Y., Li, X., Gao, F., Chen, Y., Chen, Z., 2024. Experimental investigation into gas production from methane hydrate in sediments with different contents of illite clay by depressurization. Energy 296, 131181. https://doi.org/10.1016/i.energy.2024.131181.
- Dai, S., Seol, Y., 2014. Water permeability in hydrate-bearing sediments: A pore-scale study. Geophys. Res. Lett. 41 (12), 4176–4184. https://doi.org/10.1002/2014C1.060535
- Dong, C., Wang, L., Zhou, Y., Huang, F., Song, Y., Zhou, B., Xu, H., 2020. Microcosmic retaining mechanism and behavior of screen media with highly argillaceous fine sand from natural gas hydrate reservoir. J. Nat. Gas Sci. Eng. 83, 103618. https://doi.org/10.1016/j.jngse.2020.103618.
- Dong, H., Blunt, M.J., 2009. Pore-network extraction from micro-computerized-tomography images. Phys. Rev. E 80 (3), 036307. https://doi.org/10.1103/PhysRevE.80.036307.
- Han, G., Kwon, T.-H., Lee, J.Y., Kneafsey, T.J., 2018. Depressurization-induced fines migration in sediments containing methane hydrate: X-ray computed tomography imaging experiments. J. Geophys. Res. Solid Earth 123 (4), 2539–2558. https://doi.org/10.1002/2017JB014988.
- Hou, J., Ji, Y., Zhou, K., Liu, Y., Wei, B., 2018. Effect of hydrate on permeability in porous media: Pore-scale micro-simulation. Int. J. Heat Mass Tran. 126, 416–424. https://doi.org/10.1016/j.ijheatmasstransfer.2018.05.156.
- Johnson, A., Patil, S., Dandekar, A., 2011. Experimental investigation of gas-water relative permeability for gas-hydrate-bearing sediments from the Mount Elbert gas hydrate stratigraphic test well, Alaska North Slope. Mar. Petrol. Geol. 28 (2), 419—426. https://doi.org/10.1016/j.marpetgeo.2009.10.013.
  Johnson, E.F., Bossler, D.P., Bossler, V.O.N., 1959. Calculation of relative permeability
- Johnson, E.F., Bossler, D.P., Bossler, V.O.N., 1959. Calculation of relative permeability from displacement experiments. Trans. AIME 216 (1), 370—372. https://doi.org/ 10.2118/1023-G.
- Katagiri, J., Konno, Y., Yoneda, J., Tenma, N., 2017. Pore-scale modeling of flow in particle packs containing grain-coating and pore-filling hydrates: Verification of a Kozeny—Carman-based permeability reduction model. J. Nat. Gas Sci. Eng. 45, 537—551. https://doi.org/10.1016/j.jngse.2017.06.019.
- Kleinberg, R.L., Flaum, C., Griffin, D.D., Brewer, P.G., Malby, G.E., Peltzer, E.T., Yesinowski, J.P., 2003. Deep sea NMR: Methane hydrate growth habit in porous

- media and its relationship to hydraulic permeability, deposit accumulation, and submarine slope stability. J. Geophys. Res. Solid Earth 108 (B10), 2508. https://doi.org/10.1029/2003|B002389.
- Konno, Y., Jin, Y., Uchiumi, T., Nagao, J., 2013. Multiple-pressure-tapped core holder combined with X-ray computed tomography scanning for gas—water permeability measurements of methane-hydrate-bearing sediments. Rev. Sci. Instrum. 84 (6), 064501. https://doi.org/10.1063/1.4811379.
- Lei, L., Seol, Y., Choi, J.-H., Kneafsey, T.J., 2019. Pore habit of methane hydrate and its evolution in sediment matrix—Laboratory visualization with phase-contrast micro-CT. Mar. Petrol. Geol. 104, 451–467. https://doi.org/10.1016/ i.marpetgeo.2019.04.004.
- Lenhard, R.J., Parker, J.C., 1987. A model for hysteretic constitutive relations governing multiphase flow: 2. Permeability-saturation relations. Water Resour. Res. 23 (12), 2197—2206. https://doi.org/10.1029/WR023i012p02197.
- Li, J.F., Ye, J.L., Qin, X.W., Qiu, H.J., Wu, N.Y., Lu, H.L., Xie, W.W., Lu, J.A., Peng, F., Xu, Z.Q., Lu, C., Kuang, Z.G., Wei, J.G., Liang, Q.Y., Lu, H.F., Kou, B.B., 2018. The first offshore natural gas hydrate production test in South China Sea. Chin. Geol. 1 (1), 5–16. https://doi.org/10.31035/cg2018003.
- Lu, C., Xia, Y., Sun, X., Bian, H., Qiu, H., Lu, H., Luo, W., Cai, J., 2019. Permeability evolution at various pressure gradients in natural gas hydrate reservoir at the Shenhu Area in the South China Sea. Energies 12 (19), 3688. https://doi.org/ 10.3390/en12193688
- Lu, C., Xia, Y., Qin, X., Ma, C., Bian, H., Xing, D., Lu, H., 2022. Micro- and nanoscale pore structure characterization and mineral composition analysis of clayey-silt hydrate reservoir in South China Sea. Geofluids 2022, 2837193. https://doi.org/ 10.1155/2022/2837193.
- Lu, C., Qin, X., Sun, J., Wang, R., Cai, J., 2023. Research progress and scientific challenges in the depressurization exploitation mechanism of clayey-silt natural gas hydrates in the northern South China Sea. Adv. Geo-Energy Res. 10 (1), 14–20. https://doi.org/10.46690/ager.2023.10.03.
- Mahabadi, N., Dai, S., Seol, Y., Sup Yun, T., Jang, J., 2016. The water retention curve and relative permeability for gas production from hydrate-bearing sediments: Pore-network model simulation. Geochem. Geophys. Geosyst. 17 (8), 3099–3110. https://doi.org/10.1002/2016GC006372.
- Makogon, Y.F., Holditch, S.A., Makogon, T.Y., 2007. Natural gas-hydrates—A potential energy source for the 21st Century. J. Petrol. Sci. Eng. 56 (1–3), 14–31. https://doi.org/10.1016/j.petrol.2005.10.009.
- Parker, J.C., Lenhard, R.J., Kuppusamy, T., 1987. A parametric model for constitutive properties governing multiphase flow in porous media. Water Resour. Res. 23 (4), 618–624. https://doi.org/10.1029/WR023i004p00618.
- Qin, X., Liang, Q., Ye, J., Yang, L., Qiu, H., Xie, W., Liang, J., Lu, J.a., Lu, C., Lu, H., Ma, B., Kuang, Z., Wei, J., Lu, H., Kou, B., 2020. The response of temperature and pressure of hydrate reservoirs in the first gas hydrate production test in South China Sea. Appl. Energy 278, 115649. https://doi.org/10.1016/j.apenergy.2020.115649.

- Seol, Y., Kneafsey, T.J., 2009. X-ray computed-tomography observations of water flow through anisotropic methane hydrate-bearing sand. J. Petrol. Sci. Eng. 66 (3–4), 121–132. https://doi.org/10.1016/j.petrol.2009.01.008.
- Singh, H., Myshakin, E.M., Seol, Y., 2019. A nonempirical relative permeability model for hydrate-bearing sediments. SPE J. 24 (2), 547–562. https://doi.org/10.2118/ 193996-PA.
- Sloan, E.D., 2003. Fundamental principles and applications of natural gas hydrates. Nature 426, 353–359. https://doi.org/10.1038/nature02135.
- Uchida, T., Lu, H., Tomaru, H., 2004. Subsurface occurrence of natural gas hydrate in the Nankai Trough Area: Implication for gas hydrate concentration. Resour. Geol. 54 (1), 35–44. https://doi.org/10.1111/j.1751-3928.2004.tb00185.x.
- van Genuchten, M.T., 1980. A closed-form equation for predicting the hydraulic conductivity of unsaturated soils. Soil Sci. Soc. Am. J. 44 (5), 892–898. https://doi.org/10.2136/sssai1980.03615995004400050002x.
- Waite, W.F., Santamarina, J.C., Cortes, D.D., Dugan, B., Espinoza, D.N., Germaine, J., Jang, J., Jung, J.W., Kneafsey, T.J., Shin, H., Soga, K., Winters, W.J., Yun, T.-S., 2009. Physical properties of hydrate-bearing sediments. Rev. Geophys. 47 (4), RG4003. https://doi.org/10.1029/2008RG000279.
- Wang, L., Shen, S., Wu, Z., Wu, D., Li, Y., 2024. Strength and creep characteristics of methane hydrate-bearing clayey silts of the South China Sea. Energy 294, 130789. https://doi.org/10.1016/j.energy.2024.130789.
- 130789. https://doi.org/10.1016/j.energy.2024.130789.
  Winters, W., Walker, M., Hunter, R., Collett, T., Boswell, R., Rose, K., Waite, W., Torres, M., Patil, S., Dandekar, A., 2011. Physical properties of sediment from the Mount Elbert gas hydrate stratigraphic test well, Alaska North Slope. Mar. Petrol. Geol. 28 (2) 361–380. https://doi.org/10.1016/j.marnetgeo.2010.01.008
- Petrol. Geol. 28 (2), 361–380. https://doi.org/10.1016/j.marpetgeo.2010.01.008. Xia, Y., Xu, S., Lu, C., Andersen, P.Ø., Cai, J., 2023. Characterization and capillary pressure curve estimation of clayey-silt sediment in gas hydrate reservoirs of the South China Sea. Adv. Geo-Energy Res. 10 (3), 200–207. https://doi.org/10.46690/ager.2023.12.06.
- Xia, Y., Elsworth, D., Cai, J., Lu, C., Ma, C., 2024. Pore-scale water—gas distribution and gas permeability of natural gas hydrate reservoirs in the South China Sea. Geosci. Front. 15 (4), 101816. https://doi.org/10.1016/j.gsf.2024.101816.
- Ye, J., Qin, X., Xie, W., Lu, H., Ma, B., Qiu, H., Liang, J., Lu, J.a., Kuang, Z., Lu, C., Liang, Q., Wei, S., Yu, Y., Liu, C., Li, B., Shen, K., Shi, H., Lu, Q., Li, J., Kou, B., Song, G., Li, B., Zhang, H.e., Lu, H., Ma, C., Dong, Y., Bian, H., 2020. Main progress of the second gas hydrate trial production in the South China Sea. Geol. Chin. 47 (3), 557–568. https://doi.org/10.12029/gc20200301 (in Chinese).
- https://doi.org/10.12029/gc20200301 (in Chinese).

  Zhang, P., Tian, S., Zhang, Y., Li, G., Wu, X., Wang, Y., 2021. Production simulation of natural gas hydrate using radial well depressurization. Petrol. Sci. Bull. 6 (3), 417–428. https://doi.org/10.3969/j.issn.2096-1693.2021.03.033 (in Chinese).
- Zhang, W., Liang, J., Lu, J.a., Wei, J., Su, P., Fang, Y., Guo, Y., Yang, S., Zhang, G., 2017. Accumulation features and mechanisms of high saturation natural gas hydrate in Shenhu Area, northern South China Sea. Petrol. Explor. Dev. 44 (5), 708–719. https://doi.org/10.1016/S1876-3804(17)30082-4.